2 × 2 MONOLITHIC MIRROR CAMERA DESIGN FOR MID-IR

by

Jonghwan Kim

A Thesis Submitted to the Faculty of the

JAMES C. WYANT COLLEGE OF OPTICAL SCIENCES

In Partial Fulfillment of the Requirements

For the Degree of

MASTER OF SCIENCE

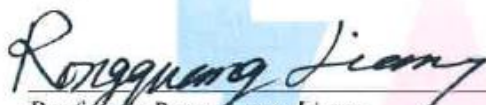In the Graduate College

THE UNIVERSITY OF ARIZONA

2021

THE UNIVERSITY OF ARIZONA
GRADUATE COLLEGE

As members of the Master's Committee, we certify that we have read the thesis prepared by **Jong-hwan Kim**, titled *2 X 2 Monolithic Mirror Camera for MID-IR* and recommend that it be accepted as fulfilling the thesis requirement for the Master's Degree.
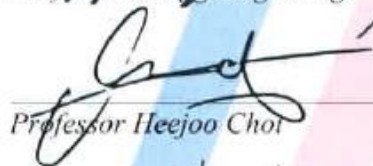
_____   Date: 5/18/2021
Professor Daewook Kim

_____   Date: 05/18/2021
Professor Rongguang Liang

_____   Date: 05/18/2021
Professor Heejoo Choi

_____   Date: 05/18/2021
Professor Hasul Kim

Final approval and acceptance of this thesis is contingent upon the candidate's submission of the final copies of the thesis to the Graduate College.

I hereby certify that I have read this thesis prepared under my direction and recommend that it be accepted as fulfilling the Master's requirement.

_____   Date: 5/18/2021
Professor Daewook Kim
Master's Thesis Committee Chair
Wyant College of Optical Sciences

ACKNOWLEDGMENTS

DEDICATION

To my beloved wife and daughter: Hueyoung and Soyool

TABLE OF CONTENTS

LIST OF FIGURES

LIST OF TABLES

ABSTRACT

This paper presents the design of a mid-infrared (mid-IR) 2×2 monolithic mirror camera having an entrance pupil diameter of 259 mm, a focal length of 537.253 mm, and a 1° field-of-view (FoV). This camera shows optical performance with 15 μm spot radius of the given FoV requirements for IR array of detectors (30 μm pixel pitch). Specifically designed for mid-IR sensing, the camera uses an IR detector with a quantum interband cascade structure of InAs/GaSb type-II superlattice (T2SL) materials, which was developed at the physics laboratory of Chonnam National University in South Korea

This camera design contained only two monolithic mirrors, one consisting of two surfaces with different radius of curvature. Therefore, this design has a compact and simple structure; hence, easy to manufacture, test, and align. The optical design for the camera inspired by the Vera C. Rubin Observatory's Large Synoptic Survey Telescope (LSST), an improved Paul-Baker three-mirror system with three refractive lenses and a color filter. Considering the need to add cooling and signal processing equipment behind the detector, we decided to modify the design to add a quaternary mirror instead of the camera lenses.

To determine tolerances, M2/M4 mirror substrate was misaligned, and the direction of maximum error was measured. As a result, in the range of 30 μm RMS spot radius for the three DoF, the calculated tolerances were 0.4° for X-rotation, 0.17 mm for Y-translation, and 0.03 mm for Z-translation. This outcome confirmed that Z-translation is the most sensitive of the three.

1. Introduction

In 1800, William Herschel discovered infrared (IR) radiation when a thermometer irradiated over the red-light spectrum registered a temperature increase. He found that the highest temperature reading occurred beyond the visible red spectrum, which is now called infrared [1]. IR radiation constitutes electromagnetic waves between the visible red and microwave regions within the $0.7 \sim 1000 \ \mu m$ region. Because the vibrational energy of atoms corresponds to the IR wavelengths, IR radiation has a stronger thermal effect than visible or ultraviolet radiation [2]. Figure 1.1 shows spectral distribution of infrared range and our target band ($2.5 \sim 4 \ \mu m$) included in mid-wavelength infrared (mid-IR).

This paper focuses on infrared detectors and imaging, important components in IR equipment used in various fields such as communications, medical care, weather analysis, and military surveillance. The following sections describe how IR imaging systems are used in modern technology and review the proposed camera design.
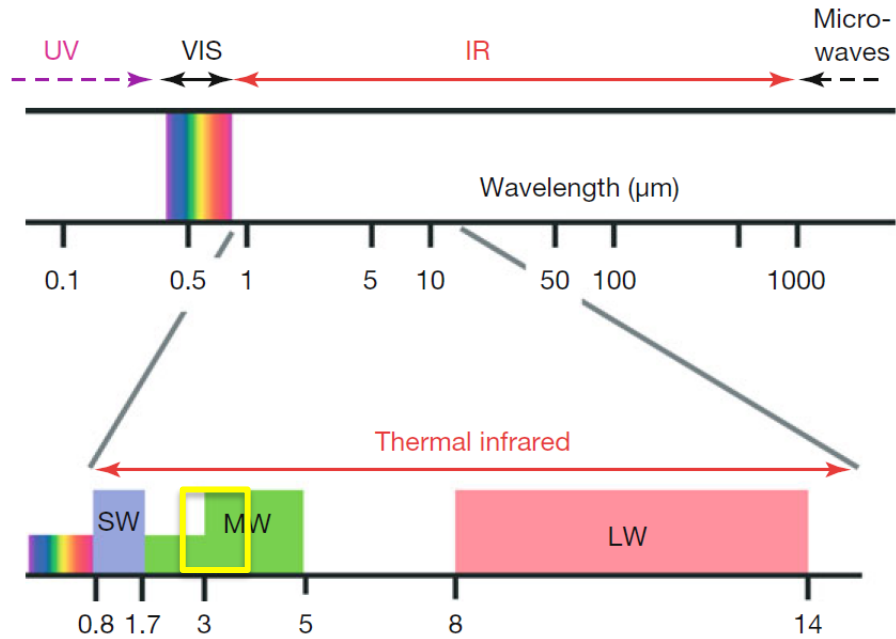
Figure 1.1. Spectral region adjacent to infrared (IR) and thermal infrared magnification [3]. The yellow box in this plot represents our target waveband.

1.1. IR imaging systems in military applications

Success in night operations has been an important military objective for many years. In an environment of limited visibility, night operations are fraught with dangers and difficulties. Military night operations have spurred IR imaging technology development. IR detectors are used to search and identify enemy forces and objects that emit heat, including humans, vehicles, and airplanes. In modern warfare, IR detection equipment is used to seek and track enemy personnel and equipment by their thermal IR radiation emission.

Early thermal IR imaging devices appeared during World War II. The U.S., U.K., and Germany have developed basic infrared sniper scope that combine near-infrared cathodes with visible phosphors to provide near-infrared converters for night combat, but the range was less than 100 meters. In addition, infrared scopes required heavy batteries and active infrared searchlights had to be mounted on flatbed trucks because of their large size [4].

Figure 1.2. Military infrared detecting devices: past and present. German infrared night-vision devices, ZG1229 (left) and 3rd Gen eLRAS3 FLIR system (right). The improvements compared to the past are following: 1) switch from active to passive system to prevent users from exposing their positions, 2) detect both long and medium wavelengths (both body temperature and heat from equipment), 3) dramatic increase in resolution and detection range [4, 5].

1.2. IR imaging systems in civil industries

  IR detectors are also used in civil industries such as industrial thermography, fire risk assessment, and medical diagnosis. IR thermal imaging is considered an efficient nondestructive test for monitor building thermal insulation by measuring the surface temperature of the building envelope from inside or outside. IR spectroscopy provides useful information on the structure of compounds. In particular, fourier transform infrared (FTIR) spectroscopy, which is used most frequently, can conduct nondestructive analysis at room temperature and pressure regardless of the target, such as organic compounds, semiconductors, or ceramics, enabling accurate data through high-resolution spectra in a short analysis time. [6].
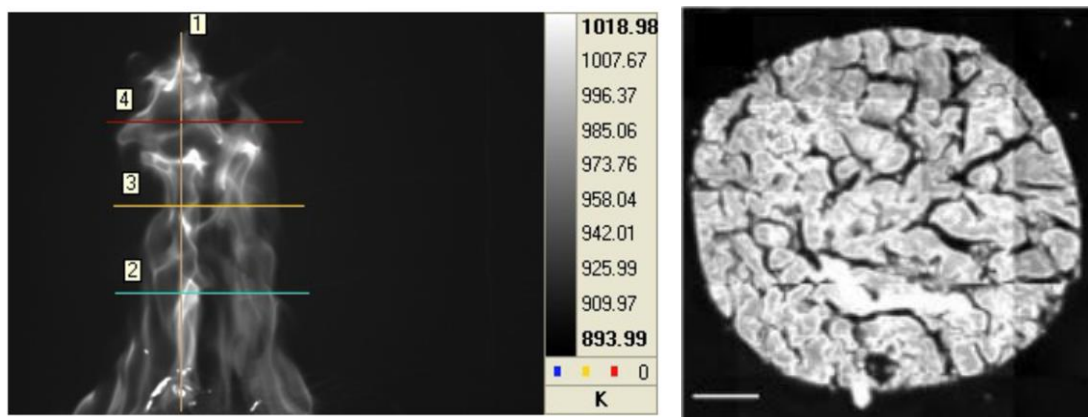
Figure 1.3. IR image of a flame (left) and a liver biopsy core (right). In the left figure, the wavelength ranges from 2.5 ~ 2.7 μm were used to show a good radiation area with high temperatures. The right figure shows the FTIR spectroscopy image of liver core at 3,286 cm^{-1} wavenumbers [7, 8].

1.3. Requirements for field applications

  Adoption of IR system in practical field faces many challenges, and the representative items are following: 1) noise equivalent difference temperature (the temperature change in a scene required to produce a signal equal to the RMS noise), 2) pixel and chip size for

resolving changes in spatial resolution, 3) uniformity of detector responsivities (affecting the complexity of the IR system), and 4) identification and detection range (a function of infrared system resolution and sensitivity) [9].

J. A. Sobrino examined thermal infrared imaging applications and the requirements for high-resolution imaging application [10]. He categorized application requirements in more than 30 fields, divided into three areas: 1) land and solid earth, 2) health and hazards, and 3) security and surveillance. In his study, Sobrino selected ten main factors that he treated as requirements for IR device design: 1) application and source, 2) earth observing (EO) level 2/3 products, 3) spatial resolution, 4) geographical coverage, 5) temporal resolution, 6) accuracy, 7) algorithms, 8) thermal infrared spectral resolution, 9) other spectral ranges, and 10) supporting data.

According to A. Rogalski, future applications of IR detector systems will require the following [11]:

• Improved pixel sensitivity.

• Pixel density greater than 10^6 pixels.

• Reducing the cost of IR imaging array systems by decreasing detector cooling requirements with improved technology and integrating the detector and signal processing with more on-chip signal processing.

• Improvement of IR imaging arrays by developing multispectral detectors.

As mentioned above, researchers listed requirements for IR detectors with regard to field applications and presented their opinions on the direction of future developments. The array of detectors used in our design are in the research stage, so the place of application

has not been decided yet, but various uses are expected for military, healthcare, and process diagnosis of industrial manufacturing.

1.4. Design overview

In this study, we proposed a mid-IR camera designed only with mirrors in an on-axis structure easily manufactured using diamond turning. This IR camera design is consisted of 4 mirrors surface in two monolithic structure, and it provides several advantages in optical layout, fabrication and alignment. First, superimposing the mirrors reduces the overall length. Second, if diamond turning is used for mirror fabrication, two mirror surfaces on one substrate can be manufactured simultaneously, and the alignment accuracy is determined by diamond turning machine's precision. Finally, by putting the two simple optical surfaces in single substrate, the testing process could be implemented without extra effort such like computer generated hologram. Several optic surfaces in single diamond turning iteration have been realized by researchers. In 2018, N. Heidler used diamond turning to build the M1/M3 mirror plane of the three mirror anastigmat (TMA) telescope at the same time. Figure 1.4 shows his telescope design and single diamond turning work piece of M1 and M3 [12].
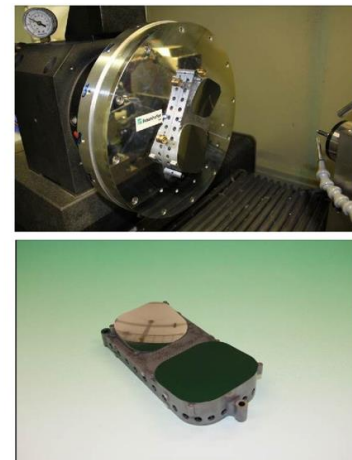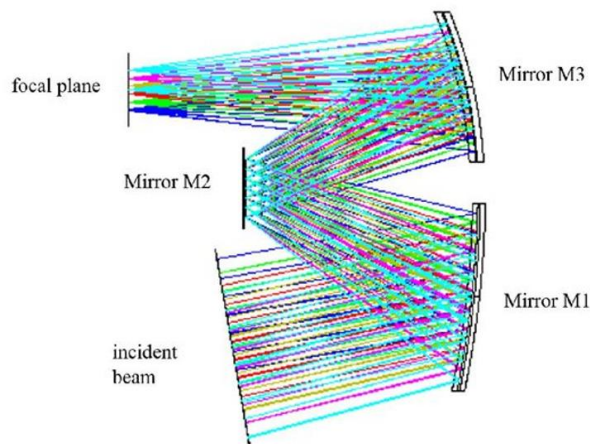
Figure 1.4. Optical design of the TMA telescope (left), M1/M3 module during (upper right) and after (lower right) diamond turning process [12]. This is an example of two mirror surfaces being manufactured simultaneously using the diamond turning.

We benchmarked the Large Synoptic Survey Telescope (LSST) of the Vera C. Rubin Observatory, as described in Section 2.2. The LSST optical design is a revised Paul-Baker 3 mirror telescope with three refractive lenses and a color filter. Same as our design, the M1 and M3 mirrors are manufactured from a single monolith, so M3's orientation towards M1 is persistent and the monolith loses six degrees of freedom, simplifies optical alignment, and allows for a compact and robust structure [13][14].

If only two mirror surfaces are used, the following limitations occur: 1) The total length of the telescope must be extended, which makes it difficult to manufacture and increases the cost. 2) Few adjustable surfaces make it difficult to balance aberrations [15].
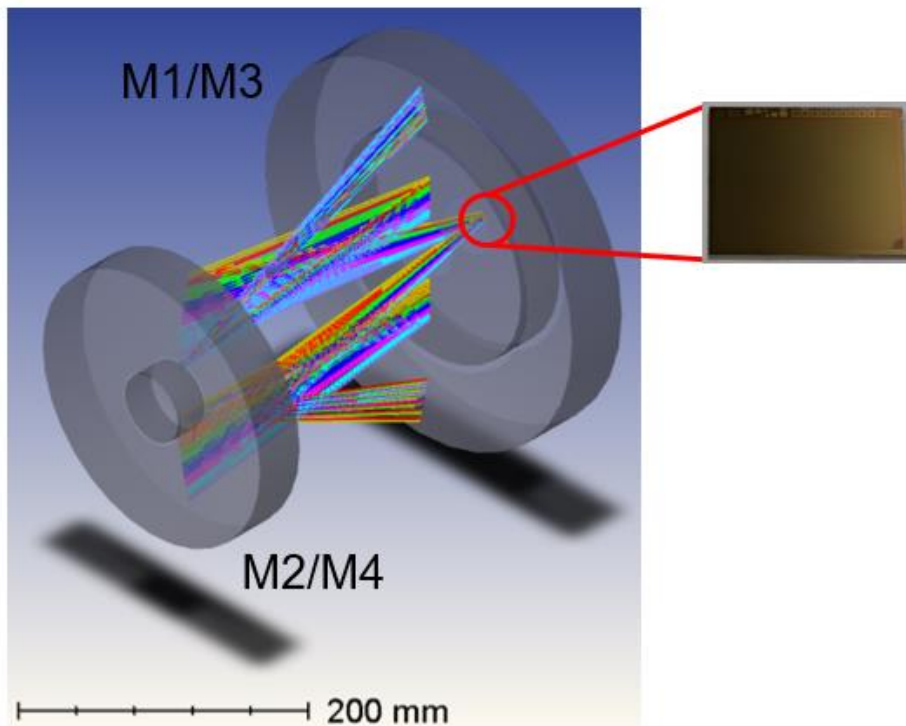
Figure 1.5. 3D layout of the 2×2 monolithic mirror camera. Working f/#: 2.07, EFFL: 537.253 mm, ENPD: 259 mm

2. Optical design

Optical design is a useful term for all the activities required to create an optical system and usually starts by considering the spatial envelope of the lens (or mirror), identifying the object/image distance and size, aperture, focal length, and aberrations. [16]. While computer programs exist that offer some lens design rules and computations, there is no closed algorithm and no computer program to design and fabricate a lens without comprehensive guidance and creativity from an optical designer [17].

This section describes the mid-IR detector used in this camera and examines how the design meets the target performance requirements.

In subsection 2.1. we examine the characteristics, operating principles, and advantages of the IR detector used in this design.

In subsection 2.2, we present the optical design procedure, list the design requirements, describe the optimization process, identify the specifications of the completed design, and examine the characteristics of the mirror surfaces constituting the design.

2.1. Mid-IR detector

First, we discuss the classification and operating principles of IR detectors, broadly divided into thermal and photon detectors. In a thermal detector, absorbed IR radiation changes the temperature of the material, and the resulting changes in the conductivity of the material generate a corresponding electrical output generally independent of the incident radiation wavelength.

In photon detectors, radiation absorption in a material occurs by an interaction with electrons attached to the lattice or impurity atoms, or with free electrons. The observed electrical output signal is due to the modified electron energy distribution [18].

Developed in 1959, the HgCdTe (MCT) detector, a typical photon detector, aims to detect $3 \sim 5~\mu m$ mid-wavelength infrared (mid-IR) and $8 \sim 14~\mu m$ long-wavelength infrared (long-wave IR). Mid-IR and long-wave IR have high transmission in the atmosphere owing to the low absorption by atmospheric gases such as H_2O, O_2, and CO_2, making these IR wavelengths suitable for applications in various fields [19][20]. HgCdTe detectors are commonly used because of their high quantum efficiency and their capability to detect infrared radiation in different wavelength bands by modifying the ratio of mercury and cadmium. However, HgCdTe, which is grown on top of CdZnTe substrates, is not suitable for fabricating large format IR image detectors because of its poor uniformity, difficulty in growth, and high manufacturing cost [21].

InAs/GaSb type II superlattices (T2SLs), which use group III-V chemical semiconductors, provide alternatives that can overcome the shortcomings of HgCdTe detectors. Because T2SLs grow on substrates of the matured growth technology of GaSb, their advantages include high uniformity and yield, and relatively low prices [22]. The III-V compounds, InAs, GaSb, and AlSb, used in this detector type have a small and direct energy gap, making them useful for optoelectronics [23]. Figure 2.1 shows that III-V compounds have a smaller energy gap than HgCdTe. In addition, in figure 2.2, because of the periodic heterostructures of III-V compounds, their conduction and valence bands overlap to form minibands.
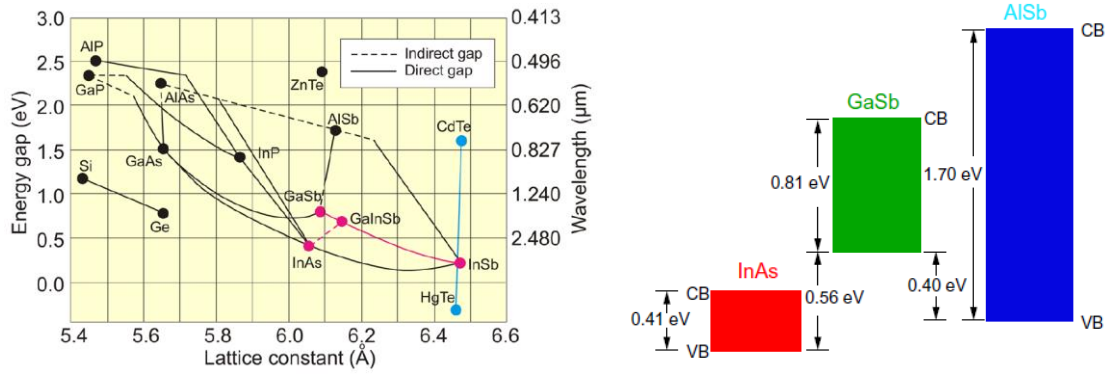
Figure 2.1. Composition and wavelength of semiconductor materials (left) [24] and band lineup of III-V compounds (InAs, GaSb, and AlSb) at room temperature (right) [25].
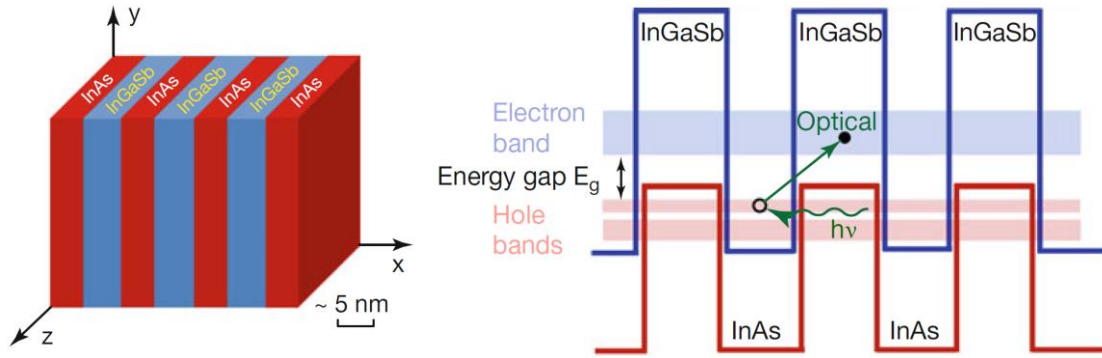
Figure 2.2. Layer structure (left) and energy band (right) of InAs/(InGa)Sb type II superlattice [26]. The blue and red lines indicate conduction and valence bands.

Introduced over the past decade, more advanced detector designs based on multistage detection, now known as cascade infrared detectors (CIDs), overcome the limitations of reduced diffusion length, effectively increasing absorption efficiency. CIDs include multiple discrete absorbers shorter than or narrower than the diffusion length [27].

Figure 2.3 shows an example of a CID band structure diagram, in which arrows indicate carrier transport. The InAs/GaSb T2SLs absorb incident photons to form electron–hole pairs. The electrons diffuse into the hole barrier where they are transferred to the next level of the valence band [28].
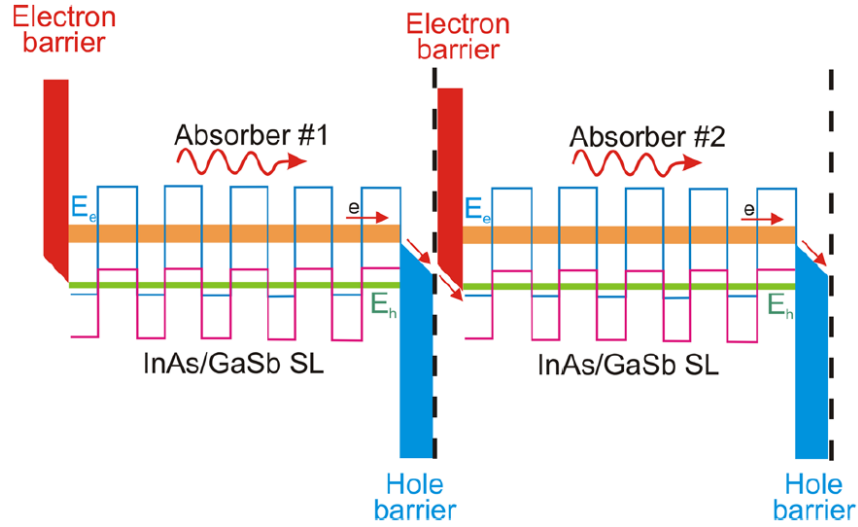
Figure 2.3. Band diagram of CIDs with 2 stages [29]. This is a plot to understand the principles of how CIDs work and is different from the detector's energy band used in this design.

Figure 2.4 shows the heterostructure of each pixel of the IR array of detectors used in this design illustrating that the seven molecular layers of InAs and eight of GaSb between the electron barrier and the hole barrier are composed of 30 periods.
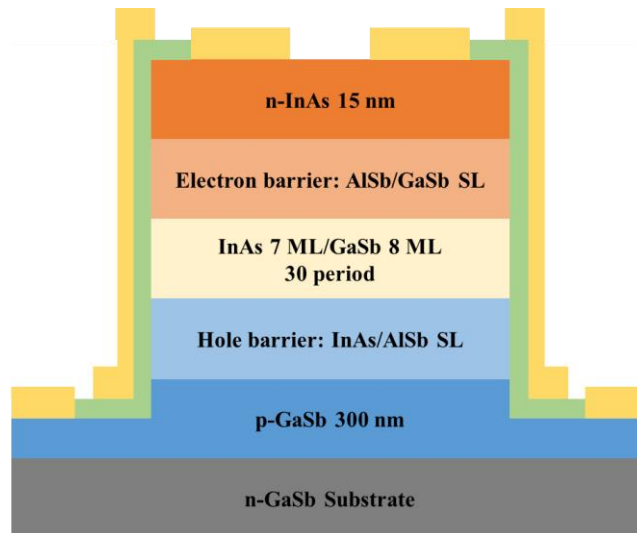
Figure 2.4. Band diagram of the heterostructure. Not depicted on a real scale [30].

Developed by the physics lab of Chonnam University, the detector of this camera design has a quantum cascade interband structure consisting of an InAs/GaSb type II superlattice. The key advantages of this detector are the high quality, high uniformity, and stability of the materials [21]. Figure 2.5 shows zoomed-in images of the array of detectors, demonstrating the good pixel alignment and Table 2.1 lists the detector specifications for the design of this camera. This array of detectors, also known as a focal plane array (FPA), was built for ISC9705 ROIC (Readout integrated circuit) compatibility which was introduced by FLIR Systems in 1997. This detector is a rectangular shape, pixel size is 24 μm and pixel spacing 6 μm, so our pixel pitch going to be 30 μm. This is the reason we are using the 15 μm, a half pixel pitch, as a criterion for all our optical evaluation [31].
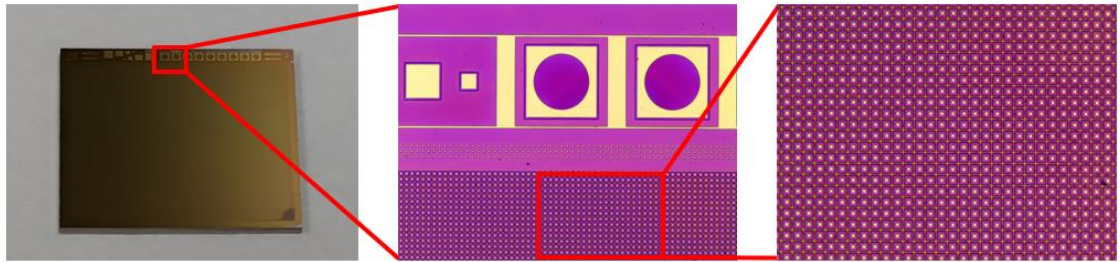
Figure 2.5. Close-up images of the detector [30].

Table 2.1. Camera detector specifications.

Parameters	Specifications
Resolution	320×256 pixels
Pixel size	$24 \times 24\ \mu m$
Pixel spacing	$6\ \mu m$
Spectral response	$2.5 \sim 4\ \mu m$
Detector size	$9.6 \times 7.68\ mm$

2.2. Compact 2 × 2 four-mirror camera design

This section details the specifications and explains the characteristics of the camera design. In our design, we followed the optical design and optimization stages in 10 processes, except the manufacture and assemble steps, as shown in Figure 2.6, that R. E. Fischer explains in his book, "Optical System Design."

1	2	3	4
Review specifications	Select starting point	Establish variables & constraints	Set performance error function

5	6	7	8
Optimize	Evaluate performance	Repeat steps 3, 5, & 6	Split elements, modify glasses, optimize repeat 3, 5, & 6

9	10	11	12
If spec not met, return to step 2	Tolerance & error budget	Element prints, design mechanics	Assemble & test
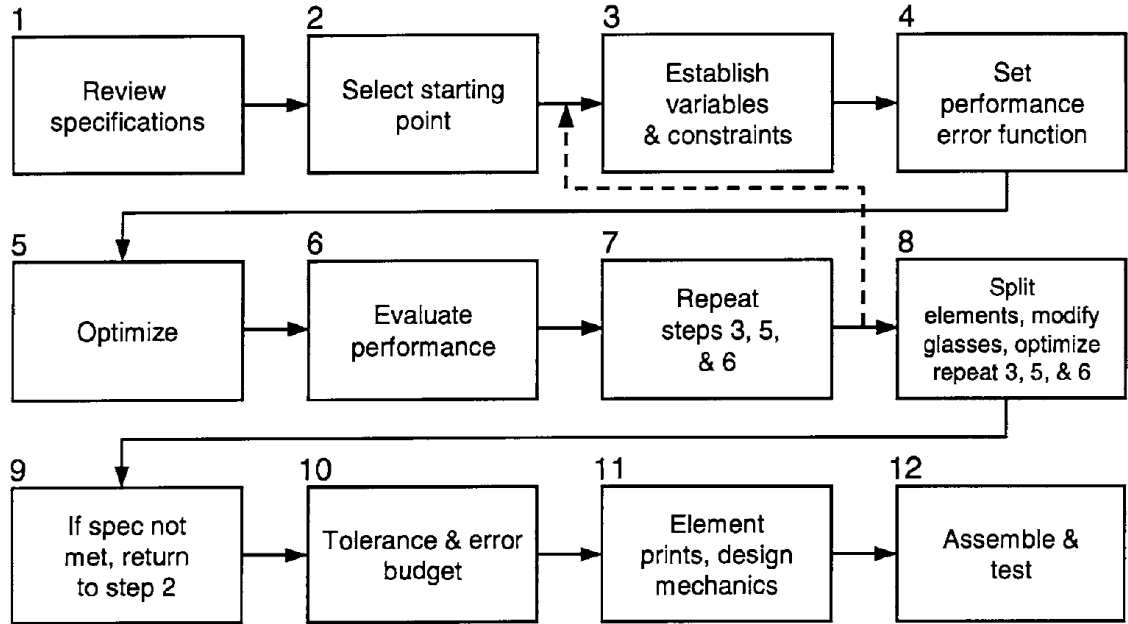
Figure 2.6. Optical design and optimization procedure [32].

For stage 1, we selected the following requirements, listed in Table 2.2, to achieve our design goal. The outer diameter was selected considering the size of the array of detectors, including the cooling and signal processing equipment.

Table 2.2. Requirement specifications.

Parameters	Targets	Note
RMS spot radius	<15 μm	0.5 Pixel pitch
Outer diameter	300 mm	size of the FPA (including cooling and signal process equipment)
Number of substrates	2	Easy to manufacture and align
Image size	$9.6 \times 7.68\ mm$	Same as FPA size
FoV	1°	Far object / high-resolution imaging

For stage 2, we selected the Large Synoptic Survey Telescope (LSST) as the starting point for the design. LSST uses three unique mirror designs to provide a 3.5° field of view. The circular 8.4 m primary mirror (M1) and 5.1 m tertiary mirror (M3) share a single monolithic substrate made by the Richard F. Caris Mirror Lab in Tucson, Arizona [33]. Considering the need to add cooling and signal processing equipment behind the detector, we decided to modify the design to add a fourth mirror instead of the camera lenses. This was accomplished by using the "scale lens" tap in Zemax to match the desired size and add a mirror surface.
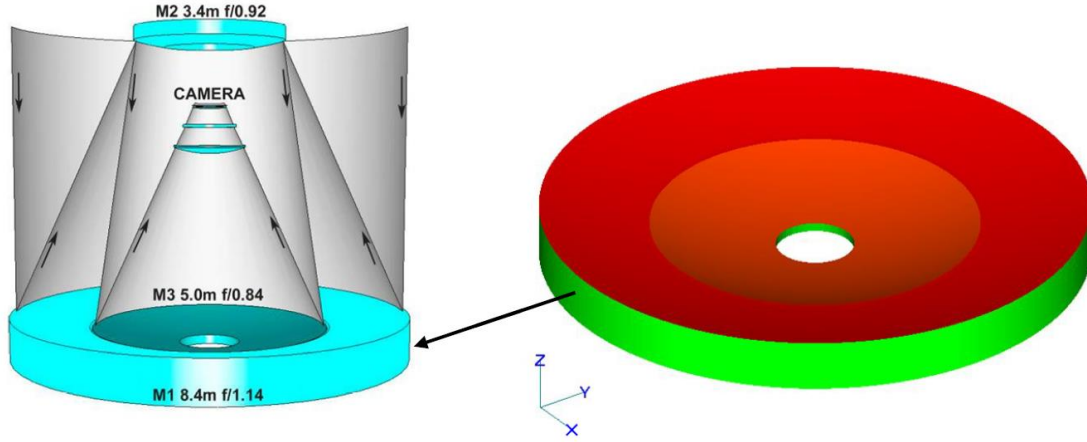
Figure 2.7. Optical layout of LSST (left) and isometric view of M1/M3 (right) [33].

Next, the variables (radii, conic constants), and constraints (length, detector size, FoV) were established (stage 3). We then designated the RMS spot radius as the performance error function (stage 4). The RMS spot radius was set to a target of 15 μm or less, which is half the pixel pitch, thereby the spot of the system can accommodate a single pixel.

Subsequently, we optimized the design (stage 5) and evaluated its performance (stage 6). This process was repeated until the specifications were met (stages 7 ~ 9), and we checked the tolerance (stage 10). Figure 2.8 shows the layout of our completed design after several optimizations.
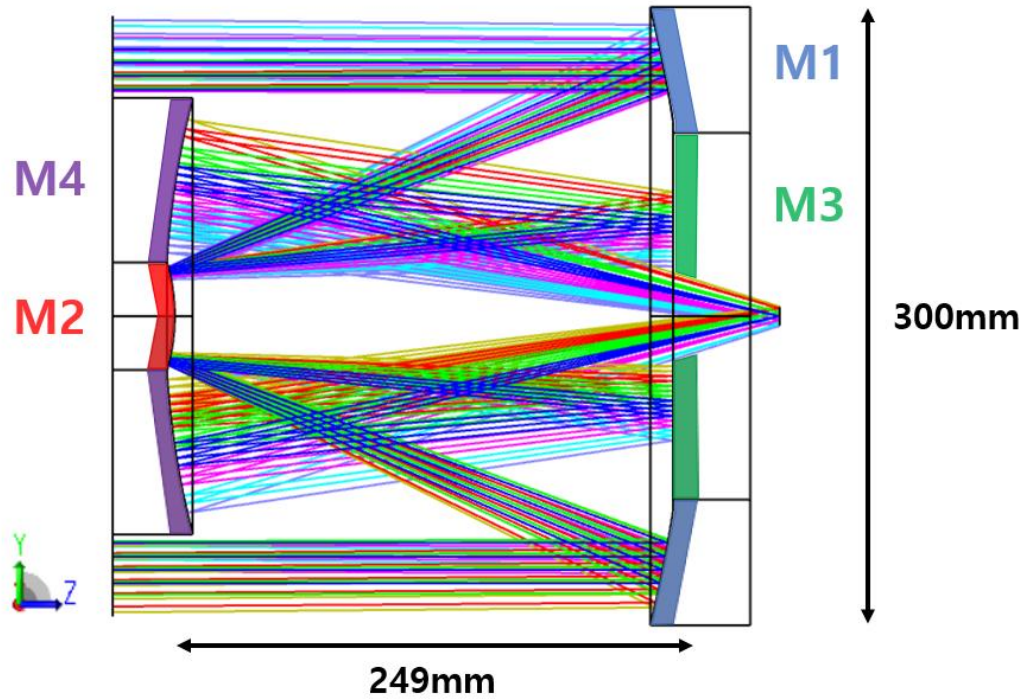
Figure 2.8. Cross section view of the final design.

The following describes the mirror surfaces, as listed in Table 2.3.

Table 2.3. Mirror surface properties.

	Monolithic #1		Monolithic #2	
	M1	**M3**	**M2**	**M4**
Outer / inner diameter (mm)	300 / 190	178 / 44	52 / 0	212 / 56
Radius of curvature (mm)	-611.287	Infinity (flat)	-92.006	423.633
Conic constant	-1 (parabola)	0	-0.242	-0.026

24

M1, the largest of the four mirror surfaces, has a paraboloidal surface design, making it was easy to manufacture and test. Its diameter was set to 300 mm, considering the size of the FPA cooling and signal processing unit. M3, designed to be constructed on a single substrate with M1, has a flat design for ease of manufacturing.

M2, the convex aspheric mirror and the smallest of the four mirror surfaces, was designed to be smaller than M4 to reduce the f-number. M4, the concave aspheric mirror and the last mirror surface in this design, was placed in the same plane as M2, allowing M2-M4 to be on a single substrate.

Figure 2.9 shows nine-field footprint diagrams of each mirror surface. The inner diameter and light in M3 and M4 were significantly close, having a 2 mm margin. To verify improvements converging to the specifications, the footprint diagram was checked continuously during the iterative system optimization. The footprint diagrams in Figure 2.9 also show that except the central obscuration and spider, there is no vignetting within the line field of view, which is considered an optimization parameter.
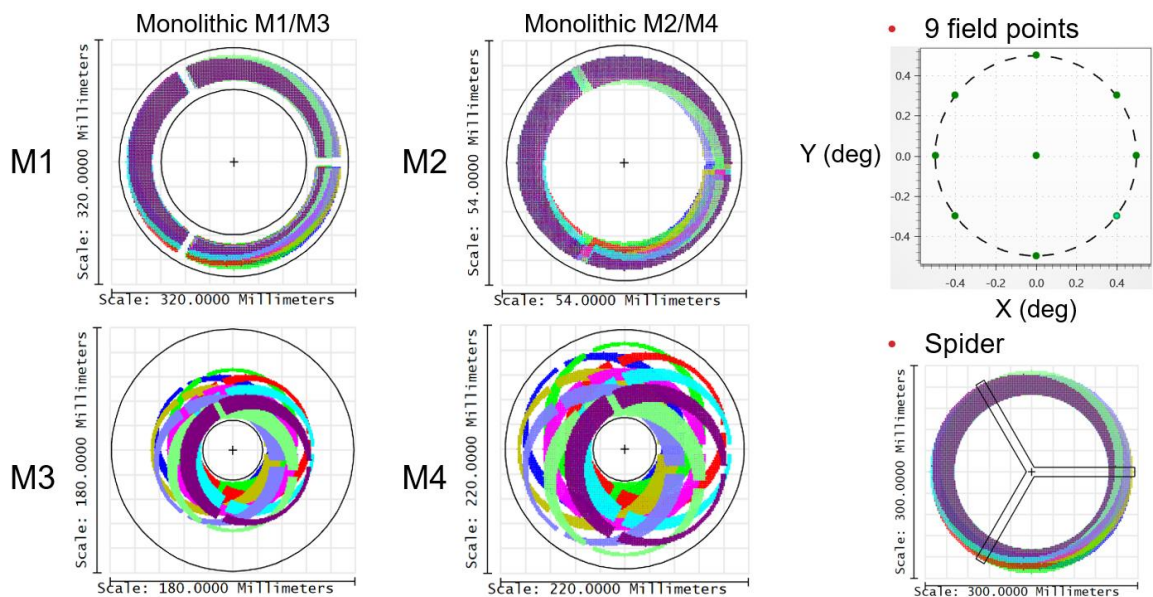
Figure 2.9. Footprint diagram of four mirror surfaces. There is a 2 mm margin in the inner circle of M3 and M4. It was confirmed that without the central obscuration and spider, there was no vignetting when the fields were ±0.5 degrees in the x, y and diagonal directions.

We compared the design specifications with the actual design and found that the other conditions were matched. However, the detector size was slightly larger than this requirement.

Table 2.4 Comparison of the specifications and the actual design.

Parameters	Targets	Results
RMS spot radius	$<15 \, \mu m$	$14.492 \, \mu m$
Outer diameter	$300 \, mm$	$300 \, mm$
Number of substrates	2	2
Image size	$9.6 \times 7.68 \, mm$	$9.38 \, mm$ (Diameter)
FoV	$1°$	$1°$

Figure 2.10 shows the size of the detector plane and 1° FoV. The optimized FoV encompasses most of the detector plane, but not the corners.
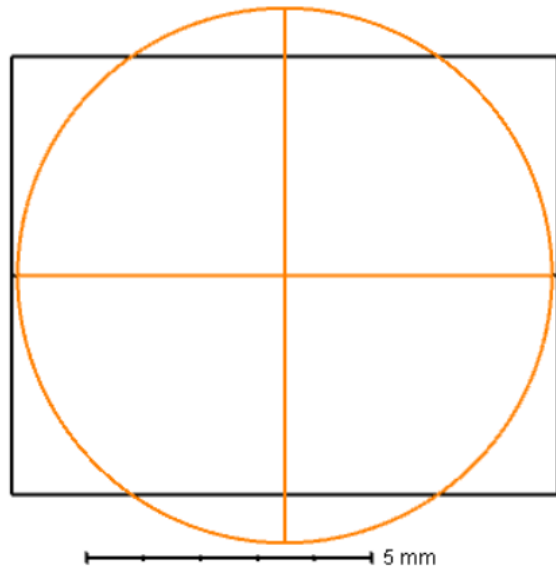
Figure 2.10. Detector (black rectangle) and 1º FoV (orange circle).

3. Optical performance

Geometric aberrations, diffraction, manufacturing and assembly errors, and other factors cause imaging system imperfections. The performance of an imaging optical system can be expressed in a variety of ways, including the modulation transfer function (MTF), encircled energy, RMS spot radius, and other criteria. System image quality or resolution depends not only on the optics, but also on the detectors, electronics, display devices, and other components that make up the system [34]. Therefore, we performed a comprehensive evaluation of the entire system.

3.1. Spot diagram

The spot diagram in Figure 3.1 shows the imaging characteristics of the optical imaging system. Spot diagrams are constructed by dividing the entrance pupil diameter (EPD) surface of the optical system into small parts, then calculating the coordinates of the point where the light passing through each part impinges on the image plane. Although functionally useful, identifying particular aberrations is difficult. If the geometric optics are acceptable, the density of the points is approximately proportional to the point spread function [35][36].

If the geometric aberrations are significantly less than the diffraction blur, the image is effectively represented on an Airy disk, which has a diameter proportional to the wavelength and the f-number. This type of optics is called diffraction-limited optics.

Figure 3.1 shows nine field points-focused spot diagrams on the detector plane. The black circle represents the Airy disk. In this diagram, the Airy radius is 8.8 μm, which is less than our pixel size.

Root mean square (RMS) and airy disk radius are defined as equations (1), (2).

$$Root\ Mean\ Square\ (RMS) = \sqrt{\frac{\sum_i[(x_i-x_c)^2+(y_i-y_c)^2]}{n}}, \qquad (1)$$

where n = number of rays,

x_i, y_i = coordinate of the ray at the image plane,

x_c, y_c = coordinate of the chief ray.

$$Airy\ disk\ radius = 1.22\lambda f/\#_W, \qquad (2)$$

where λ = wavelength,

$f/\#_W$ = working f-number = 1 / (2NA), \qquad NA: numerical aperture.
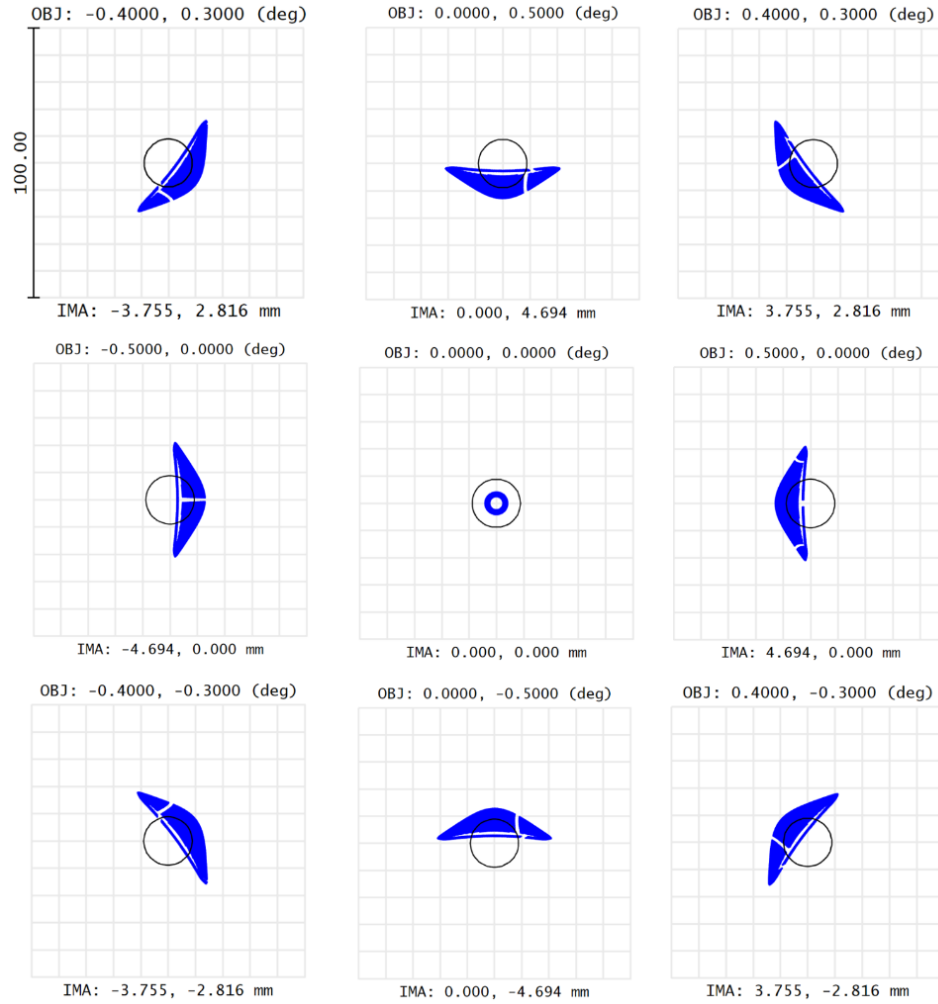
Figure 3.1. Spot diagram. Each radius is less than 15 μm in all fields.

29

Table 3.1. FoV versus RMS spot radius.

FoV (x, y)	(0°, 0°)	(0.4°, 0.3°)	(0.5°, 0°)	(0°, 0.5°)
RMS radius (μm)	3.54	14.496	14.456	14.492

3.2. Through-focus spot diagram

A through-focus spot diagram displays a spot diagram by moving the focal plane.

Figure 3.2 shows the five field points-focused spot diagrams on the detector plane through-focus. The focal plane was shifted by 200 μm between the through-focus images. This figure shows the effects of spherical aberration in the 0° field. Moreover, the spot diagrams also show that coma and astigmatism increase with increasing fields.

We could still maintain good performance throughout the entire field (RMS radius was less than 30 μm) with an approximately 50 μm slightly off-focal plane.

Figure 3.2. Through focus spot diagram.

3.3. Optical path difference

The optical path difference (OPD) of the camera refers to the difference between the optical path lengths of the ray and the chief ray. The shape of the OPD shows the extent of aberrations that exists. At 0.4° and 0.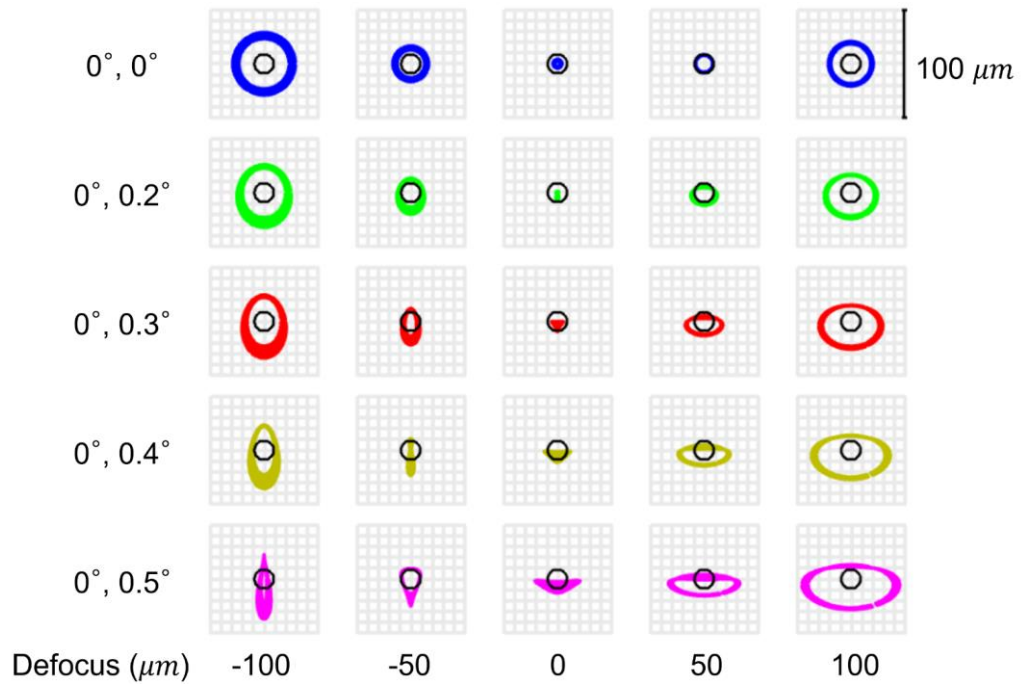5° fields, considering the asymmetry of the graph, it can be inferred that there was a comma and a distortion. Astigmatism can also be observed through the differences between the left and right graphs.

If the maximum OPD is less than 0.25 wave, the effect of aberration is considered small [37]. The OPD value was greater than 0.25 wave in a field above 0.4°, indicating significant aberrations occurred. However, since the RMS spot radius was smaller than a half pixel pitch, most of the light would stay in the pixel and therefore the detector's performance would be guaranteed.

OPL and OPD are expressed in equations (3), (4).

$$Optical\ path\ length\ (OPL) = n_1 d_1 + n_2 d_2 + \cdots (surfaces), \qquad (3)$$

where $n =$ index of refractive (constant),

$\qquad d =$ length of the ray.

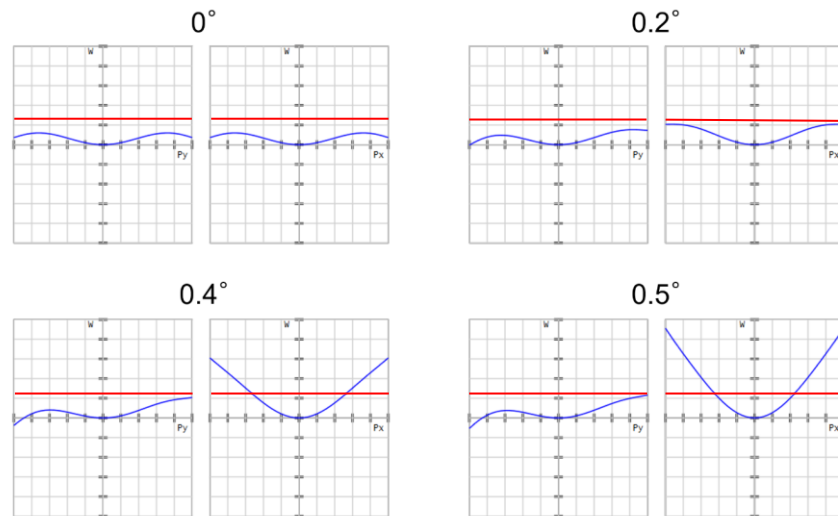$$Optical\ path\ difference\ (OPD) = n_1 d_1 - n_c d_c \qquad (4)$$

Figure 3.3. Optical path difference (OPD). Scale: ± 1 wave (wavelength: 3.5 μm). FoV is given only in the y-axis direction. The larger the field, the greater the difference between tangential ($P_x = 0$) and sagittal ($P_y = 0$) OPD, so we can see that astigmatism increases.

Table 3.2: FoV versus maximum OPD.

FoV (x, y)	(0°, 0°)	(0°, 0.2°)	(0°, 0.4°)	(0°, 0.5°)
Max. OPD (waves)	0.07	0.20	0.61	0.91

3.4. Field curvature and distortion

Field curvature refers to one of five Seidel aberrations: spherical aberration, coma, astigmatism, field curvature, and distortion, in which the plane image becomes a curved. In Figure 3.4, the graph on the left shows the field curvature, where the y-axis shows half the FoV and the x-axis shows the amount the image surface moved. Here the tangential (x_p = 0) and sagittal (y_p = 0) moved -0.06 mm at y = 0 because the positions of the paraxial image surface and image plane are different. Moreover, the aberration of the tangential is less than sagittal, similar to OPD [38].

Distortion occurs because a plane-shaped object perpendicular to the optical axis does not appear in the image plane as perpendicular to the optical axis (image magnification varies with the image height). Distortion can be divided into two types: barrel and pincushion [39]. In Figure 3.4, the graph on the right shows that the distortion increases as the field increases and has a small pincushion distortion.

Distortion can be expressed in equation (5).

$$Distortion\ (\%) = 100 \times \frac{y - y_p}{y_p}, \tag{5}$$

where $y =$ height in the image plane,

$y_p =$ paraxial height.
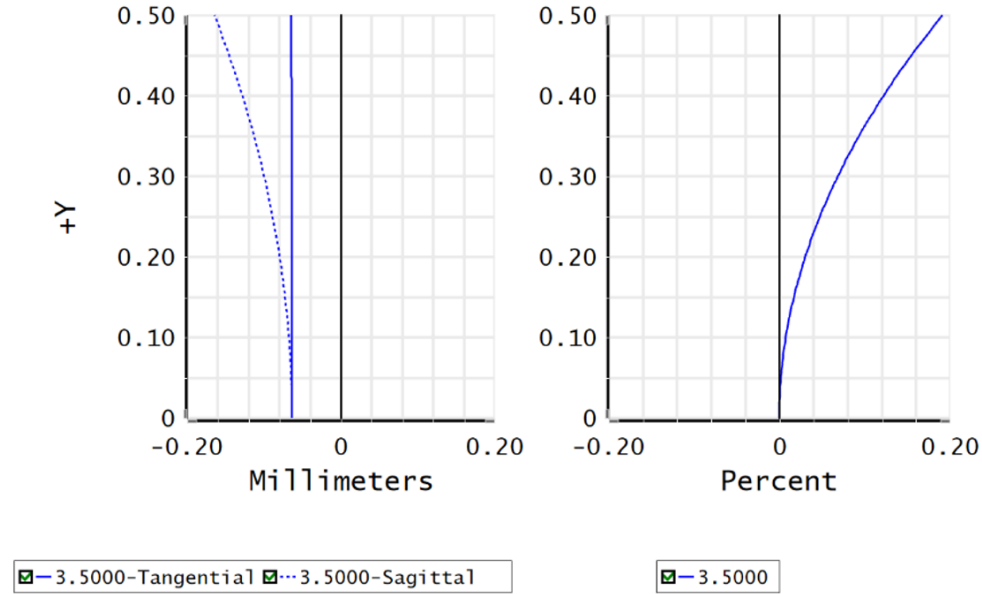
Figure 3.4. Field curvature and distortion. It has tangential (0.001 mm) and sagittal (0.101 mm) field curvature. Maximum Distortion was 0.192 %.

3.5. Seidel coefficients

Figure 3.5 shows five Seidel aberrations for each mirror surface.

M1 had considerable coma (-0.101 mm) and some astigmatism (0.023 mm) due to its parabolic geometry. M2 compensates for the M1 coma (0.096 mm) and astigmatism (-0.028 mm). However, M2 also causes substantial spherical aberration (-0.126 mm) and some field curvature (0.028 mm).

We found no aberrations in the M3 plane mirror, which is the ideal plane mirror in an optical system. This mirror only changes the direction of light travel.

M4 compensates for the M2 spherical aberration (0.106 mm), some coma, and some field curvature. As a result, the sum of aberrations is as follows: spherical (-0.020 mm), coma (0.001 mm), astigmatism (-0.006 mm), field curvature (0.018 mm), and distortion (-0.004 mm).
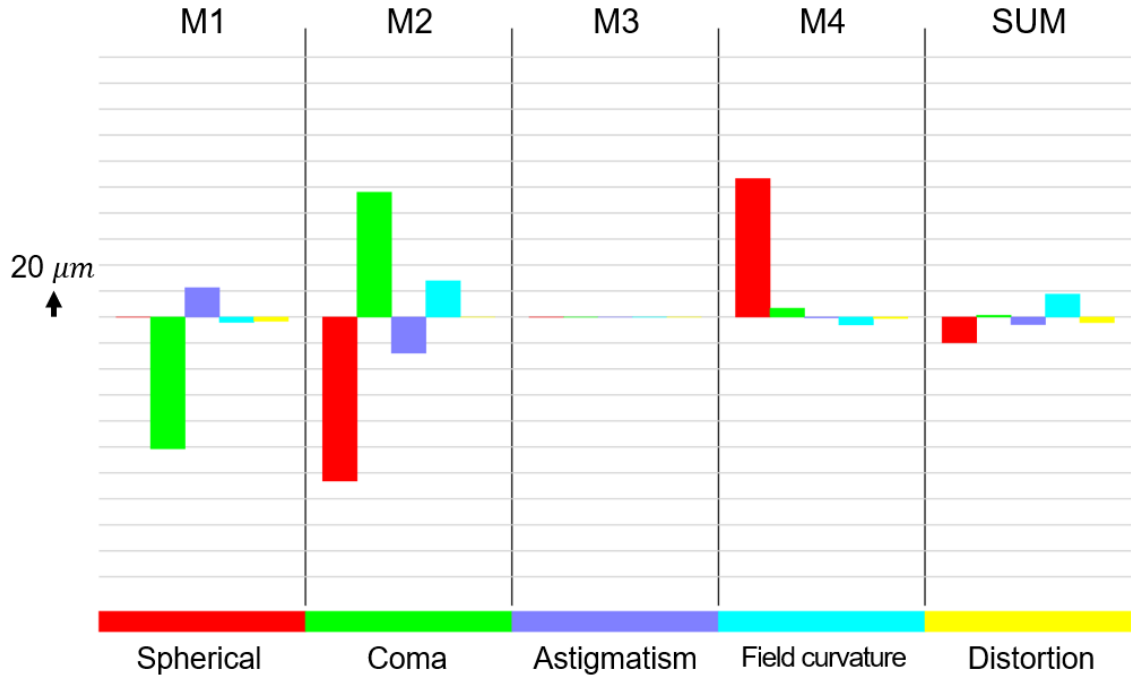
Figure 3.5. Seidel coefficients.

The equation (6) describes the wavefront expansion, a power series expansion for the wavefront aberrations and figure 3.6 shows basic wavefront deformation shapes.

$$W_{IJK} = H^I \rho^J \cos^K \theta ,\qquad (6)$$

where H = the normalized image height,

ρ, θ = polar ray coordinates in the pupil,

$W = \quad W_{020}\rho^2$ (defocus)

$+ W_{111}H\rho \cos\theta$ (wavefront tilt)

$$+ W_{040}\rho^4 \qquad \text{(spherical aberration)}$$

$$+ W_{131}H\rho^3 cos\theta \qquad \text{(coma)}$$

$$+ W_{222}H^2\rho^2 cos^2\theta \qquad \text{(astigmatism)}$$

$$+ W_{220}H^2\rho^2 \qquad \text{(field curvature)}.$$

$$+ W_{311}H^3\rho cos\theta \qquad \text{(distortion)}$$
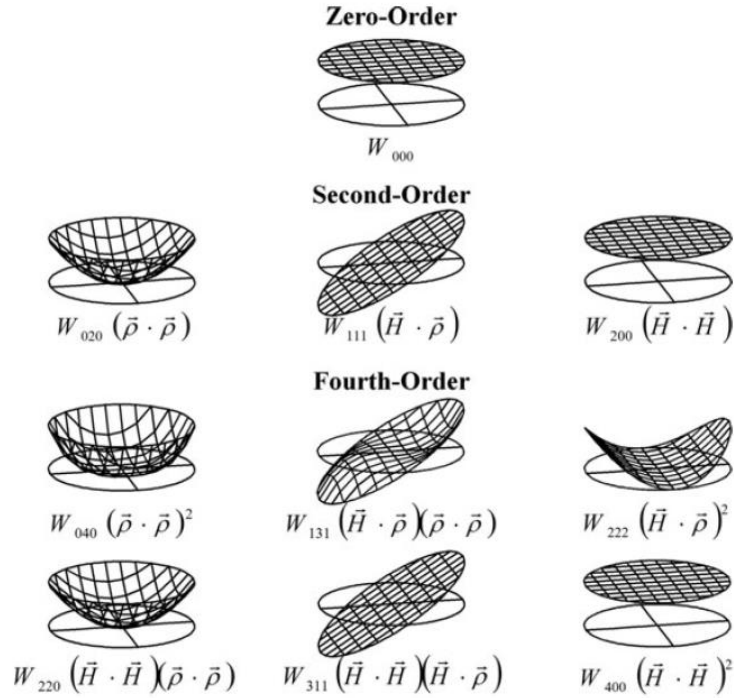
+ higher order terms.

Figure 3.6. Basic wavefront deformation shapes [40].

3.6. Point spread function

The point spread function (PSF) is the response of an imaging system to a point source, which is modeled by a two-dimensional delta function δ(x, y), i.e., an image with a sufficiently large density at the origin and zero density everywhere else. Therefore, the

point spread function represents mathematically the diffraction of an object (input) by the optical system [41].

The Strehl ratio (SR) is one of the most commonly used metrics to evaluate the performance of optical systems. It is obtained by dividing the maximum intensity measured at the focal point of the system by the maximum intensity of the ideal optical system; the ratio is 1 for an ideal system. A system with a Strehl ratio greater than 0.8 is considered to be well corrected. We observed the SR fell below 0.5 in the 0.4° field.

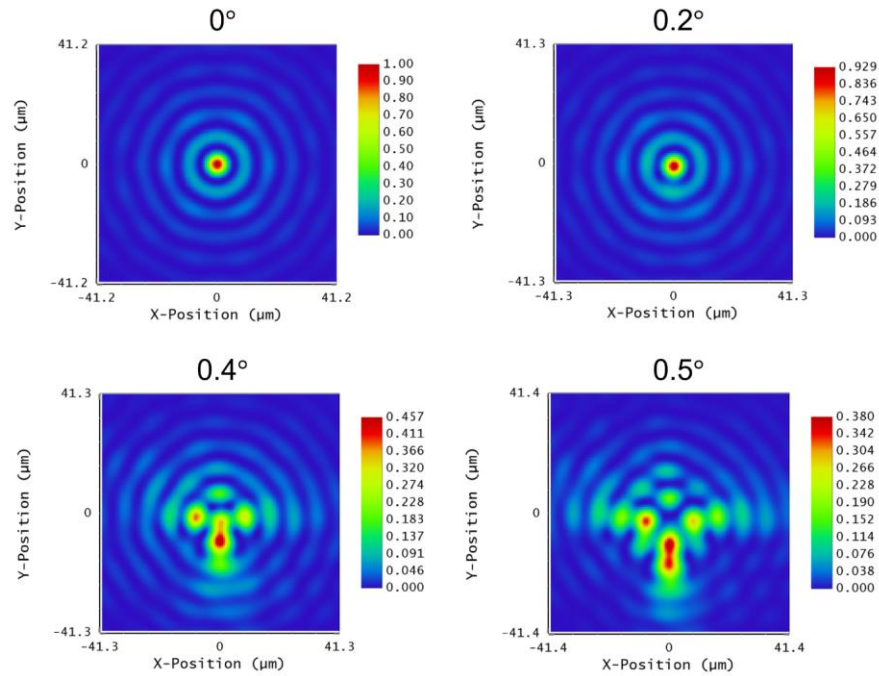**Figure 3.7. Point spread function (PSF). If the field is greater than 0.4°, the Strehl ratio becomes low.**

3.7. Longitudinal aberration

The longitudinal aberration refers to the distance from the image surface to the focal point of the zonal marginal rays along the optical axis. Calculations were performed only for the on-axis field points and zonal marginal tangential rays as a function of the pupil zone. In

36

Figure 3.8, the horizontal scale, in lens units, represents the distance from the image surface to the ray intersecting the optical axis, and the vertical scale represents the entrance pupil radius [42][43]. As shown in Figure 3.8, the distance between the image surface and focal point moves in the direction where the z-value of the optical axis increases with increasing entrance pupil radius.
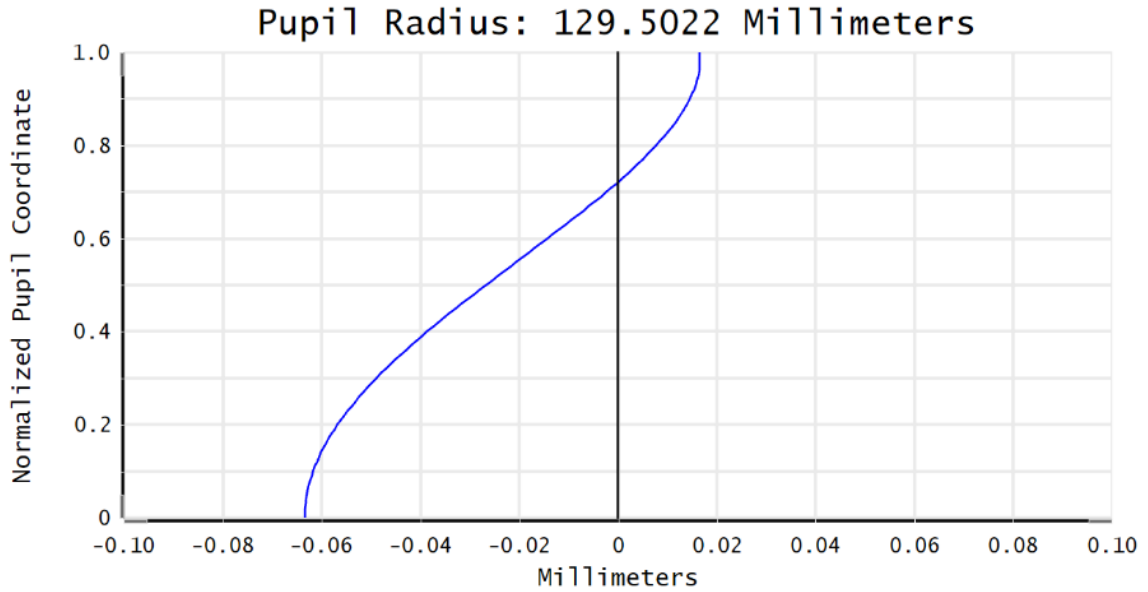
Figure 3.8. Longitudinal aberration.

3.8. Modulation transfer function (MTF)

The modulation transfer function (MTF) characterizes the optical system's contrast performance at different spatial frequencies. MTF plots are typically contrast versus spatial frequencies, with some variation in different fields, e.g., the photography industry uses contrast versus image height as the MTF plot [44].

Figure 3.9 demonstrates that for our system, the contrast decreases below 0.3 for spatial frequencies above 14 cycles/mm. MTF shows low performance, which can be attributed to the reduction in the amount of light incident due to the central obscuration [45].
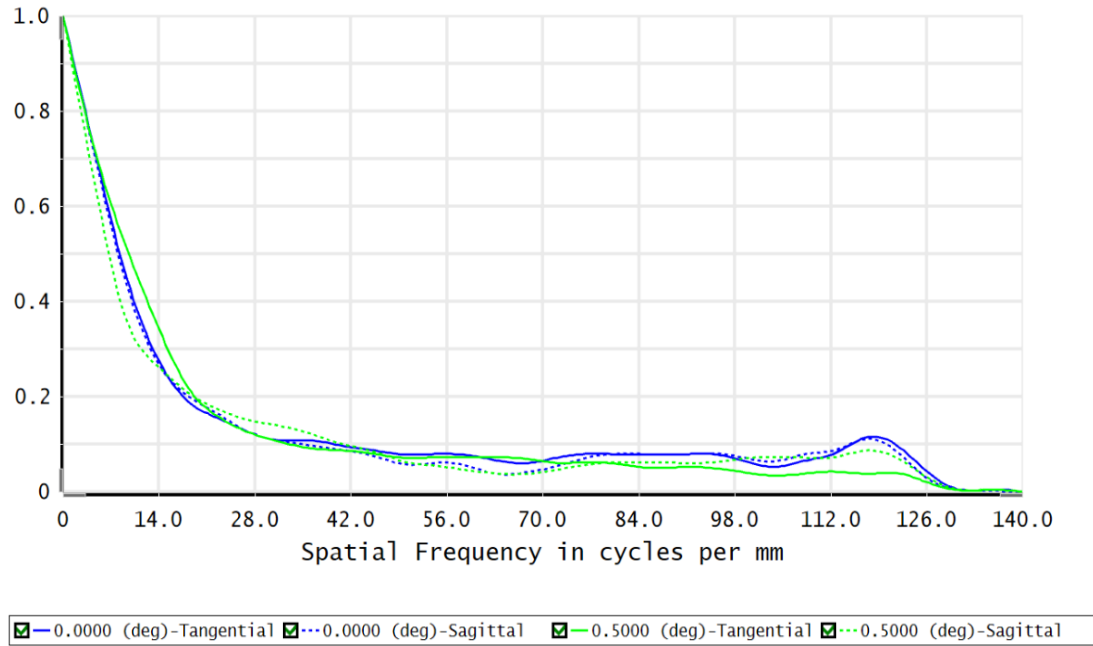
Figure 3.9. Modulation transfer function (MTF).

3.9. Encircled energy

Encircled energy refers to the amount of energy of a light beam encircled by a spot of variable radius, normalized to the total amount of energy in the beam. Consequently, the smaller the spot radius with an intensity of 1 (100%), the more ideal the system [46].

As shown in Figure 3.10, our system has encircled energy of 50% and 80% in circles of $25\ \mu m$ and $50\ \mu m$ radius, respectively. The graph shows the energy on a pixel pitch ($30\ \mu m$) is approximately 30% of the total energy.

Figure 3.10. Encircled energy.

4. Sensitivity analysis

In this section, we present a sensitivity analysis of three degrees of freedom (DoF).

This analysis evaluates the performance of the theoretical design and does not include any manufacturing error effects. While theoretical design performance is very important, hardware-related manufacturing errors and tolerances can, by definition, change and degrade actual performance.
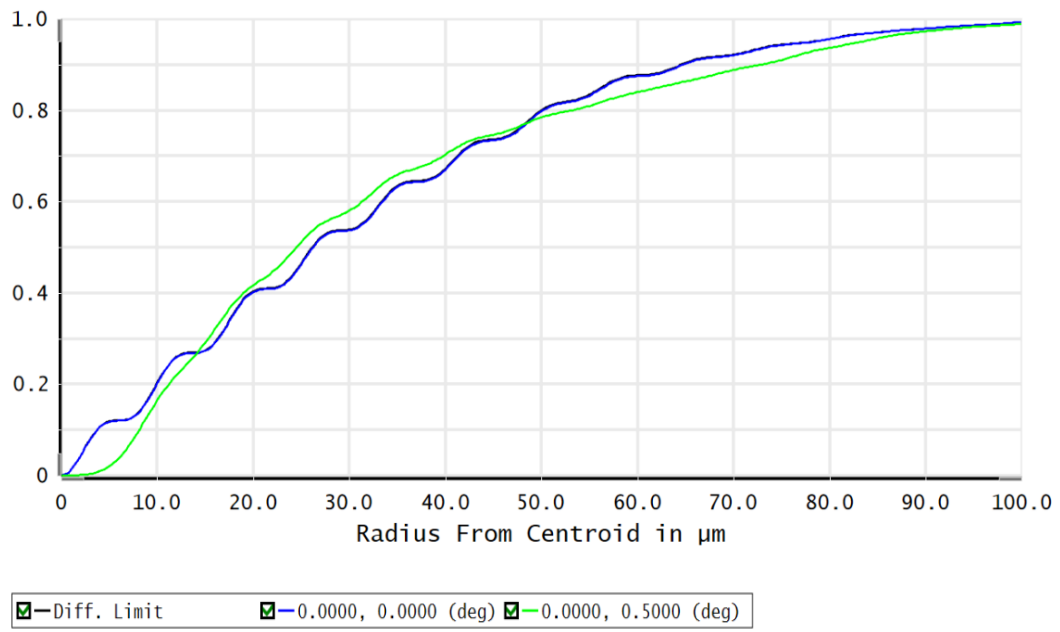
In this performance analysis, monolithic M1/M3 was fixed and used as a reference, and monolithic M2/M4 was moved in three directions. Considering the axially symmetry of the system, we determined that a complete analysis required only three DoF: X-rotation, Y-translation, and Z-translation.
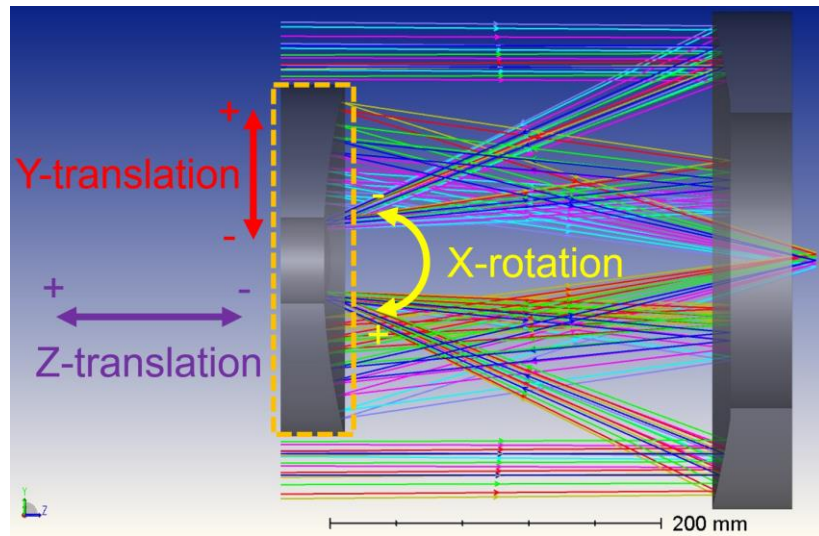
Figure 4.1. Three degrees of freedom (DoF).

We established a tolerance criterion and defined the coordinate system and. X and Y-axis were the horizontal and vertical axes of the coordinate system, and the Z-axis, same as the optical axis, was the axis of rotational symmetry.

We used RMS spot radius as the tolerance criterion, using the average of radii in four fields—[0°, 0°], [0°, 0.2°], [0°, 0.4°], and [0°, 0.5°]—with the size up to 1 pixel pitch (30 μm). Figure 4.2 and the Table 4.1 show the results of the theoretical performance analysis. Also, for comparison, we put the same size field in the x-axis and checked the results.
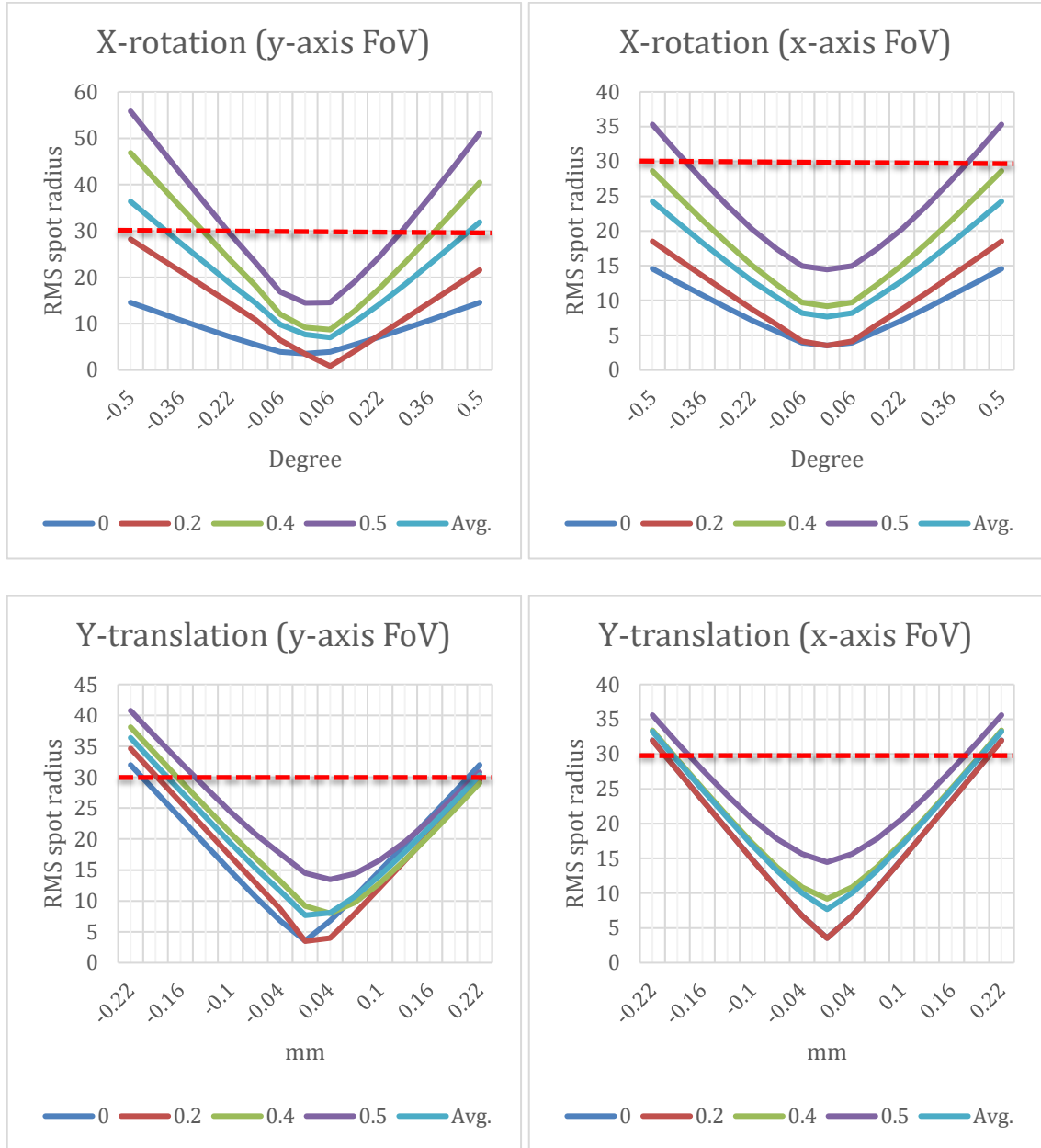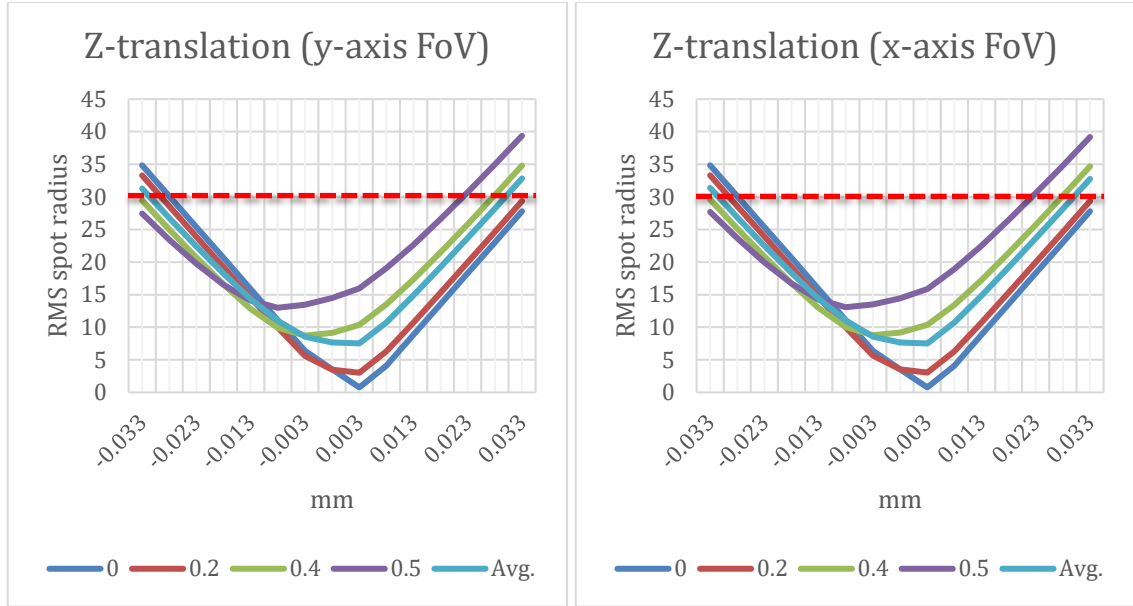
Figure 4.2. Results of analysis. These results show the y-axis on the left and the x-axis on the right, respectively, four fields and their average values. In case of x-axis, z-translation has exactly the same results, y-translation has almost the same level, and x-rotation has a larger tolerance than y-axis fields.

For X-rotation, the RMS spot radius varies the most depending on the field. Z-translation is the most sensitive of the three DoF because it has a quadrupling effect on the OPL.

The table 4.1 shows the results of the tolerance analysis and the tolerance guide for machined parts. In the case of the Z-translation, the tolerance was too small, and the machining level is precision, which requires the highest accuracy of the three DoF. This allowed us to infer that Z-translation was the most sensitive.

Table 4.1. Camera tolerances [47].

Parameters	Tolerance	Machining level
X-rotation	0.4°	Coarse dimensions (not important)
Y-translation	0.17 mm	Typical machining (low difficulty)
Z-translation	0.03 mm	Precision machining (readily available)

5. Conclusion

We designed a 2×2 monolithic mirror camera for the mid-IR range. Its optical design was inspired by the Vera C. Rubin Observatory's LSST and was customized for the mid-IR detector. It contained only two monolithic mirrors, one consisting of two surfaces with different radius of curvature. Therefore, the camera design has a compact and simple structure; hence, easy to manufacture, test, and align. This camera was designed and optimized to have an RMS spot radius of 15 μm (0.5 pixel pitch) or less in a given FoV (1°).

The optical performance evaluation confirmed that the RMS spot radius is within 15 μm in a given FoV; moreover, the spot radius was within 30 μm (1 pixel pitch), when the focus was moved within ± 50 μm. Analyzing OPD and PSF confirmed design performance deteriorated in fields greater than 0.4°.

After performing sensitivity analysis in the range of 30 μm RMS spot radius for the three DoF, the calculated tolerances were 0.4° for X-rotation, 0.17 mm for Y-translation, and 0.03 mm for Z-translation. This outcome confirmed that Z-translation is the most sensitive of the three.

Because this is a mirror-only design and has no chromatic aberrations, it has the advantage that it can be used at all wavelengths, such as IR and visible light.

In conclusion, we designed a mirror-only camera for use in mid-IR detector and conducted an optical performance evaluation and sensitivity analysis. We hope that this research will contribute to the completion of 3D modeling and actual fabrication of the camera.

REFERENCES

[1] W. Herschel. *Experiments on the refrangibility of the invisible rays of the Sun,* Phil. Trans. Roy. Soc. London 90, 284, 1800, Page 258.

[2] R. V. Prakash. *Infrared thermography*. InTech, 2012, Pages 174-175.

[3] M. Vollmer, K.-P. Möllmann. *Infrared thermal imaging: fundamentals, research and applications,* Wiley-VCH Verlag GmbH & Co. KGaA, 2018, Page 10.

[4] A. Cutolo, A. G. Mignani, A. Tajani. *Photonics for safety and security.* World Scientific Publishing Co. Pte. Ltd., 2013, Pages 229-231.

[5] A. Rogalski, K. Chrzanowski. *Infrared devices and techniques (revised).* Metrol. Meas. Syst., XXI, No. 4, 2014, Page 591.

[6] M. Vollmer, K.-P. Möllmann. *Infrared thermal imaging: fundamentals, research and applications,* Wiley-VCH Verlag GmbH & Co. KGaA, 2018, Pages 229-230, 258-263, 477.

[7] E. L. Loboda, V. V. Reyno. *Choice for research spectral response of combustion processes using the method of IR diagnostics,* Proc. SPIE, 9292, 929215, 2014, Page 7.

[8] H. Sreedhar, et al. *High-definition fourier transform infrared (FT-IR) spectroscopic imaging of human tissue sections towards improving pathology,* J. Vis. Exp., 95, 52332, 2015, Page 5.

[9] A. Rogalski, J. Antoszewski, L. Faraone. *Third-generation infrared photodetector arrays,* J. Appl. Phys., 105, 091101, 2009, Pages 6-9.

[10] J. A. Sobrino, et al. *Review of thermal infrared applications and requirements for future high-resolution sensors,* IEEE Trans. Geosci. Remote, 54, 5, 2016, Page 2.

[11] A. Rogalski. *Infrared detectors: an overview,* Infrared Physics & Technology, 43 2002, Page 207.

[12] N. Heidler, et al. *Additive manufacturing of metal mirrors for TMA telescope*, Proc. SPIE, 10692, 106920C, 2018, Pages 3-6.

[13] LSST Science Book, http://www.lsst.org/lsst/scibook, Pages 29-30.

[14] W. J. Gressler, *LSST Telescope and Site Status*, Proc. SPIE 9906, Ground-based and Airborne Telescopes VI, 99060J, 27 July 2016, Page 7.

[15] R. E. Fischer, B. Tadic-Galeb, P. R. Yoder. *Optical system design,* McGraw-Hill Education, 2008, Pages 138-146.

[16] T.Thöniss, G. Adams,C. Gerhard. *Optical system design,* Optik & Photonik, 4, 2, 30–33, 2009, Page 30.

[17] Robert R. Shannon. *The art and science of optical design,* Cambridge University Press, 1997, Page 1.

[18] A. Rogalski. *History of infrared detectors*. Opto-Electronics Review, 20, 3, 279–308, 2012, Pages 284-287.

[19] A. Rogalski, K. Chrzanowski. *Infrared devices and techniques (revised),* Metrol. Meas. Syst., XXI, No. 4, 2014, Page 566.

[20] C. Downs, T. E. Vandervelde. *Progress in infrared photodetectors since 2000,* Sensors, 13, 2013, Page 5056.

[21] A. Rogalski, P. Martyniuk, M. Kopytko. *InAs/GaSb type-II superlattice infrared detectors: future prospect,* Appl. Phys. Rev., 4, 031304, 2017, Page 18.

[22] A. Rogalski, J. Antoszewski, L. Faraone. *Third-generation infrared photodetector arrays,* J. Appl. Phys., 105, 091101, 2009, Pages 19-20.

[23] A. Rogalski. *History of infrared detectors,* Opto-Electronics Review, 20, 3, 279–308, 2012, Page 288.

[24] A. Rogalski, P. Martyniuk, M. Kopytko. *InAs/GaSb type-II superlattice infrared detectors: future prospect,* Appl. Phys. Rev., 4, 031304, 2017, Page 2.

[25] M. Razeghi. *Mid-infrared optoelectronics,* Woodhead Publishing Series in Electronic and Optical Materials, 2020, Page 380.

[26] M. Vollmer, K.-P. Möllmann. *Infrared thermal imaging: fundamentals, research and applications.* Wiley-VCH Verlag GmbH & Co. KGaA., 2018, Page 135.

[27] A. Rogalski, P. Martyniuk, M. Kopytko. *InAs/GaSb type-II superlattice infrared detectors: future prospect,* Appl. Phys. Rev, 4, 031304, 2017, Pages 9-10.

[28] Z.-B. Tian, et al. *High operating temperature interband cascade focal plane arrays,* Appl. Phys. Ltrs., 105, 051109, 2014, Page 2.

[29] A. Rogalski, P. Martyniuk, and M. Kopytko. *InAs/GaSb type-II superlattice infrared detectors: future prospect,* Appl. Phys. Rev., 4, 031304, 2017, Page 10.

[30] These figures (or images) were taken by a grant from the Basic Science Research Program through the National Research Foundation of Korea (NRF) funded by the Ministry of Science, ICT and Future Planning (2017R1A2B4007390)

[31] FLIR systems, https://www.flir.com/products/isc9705/

[32] R. E. Fischer, B. Tadic-Galeb, P. R. Yoder. *Optical system design,* McGraw-Hill Education, 2008, Pages 171-176.

[33] D. R. Neill, et al. *Final design of the LSST primary / tertiary mirror cell assembly,* Proc. SPIE, 9906, Ground-based and Airborne Telescopes, VI, 99060Q, 27 July 2016, Page 3.

[34] R. E. Fischer, B. Tadic-Galeb, P. R. Yoder. *Optical system design,* McGraw-Hill Education, 2008, Pages 179-180.

[35] Ibid. Pages 187-189.

[36] J. M. Geary. *Introduction to lens design,* Willmann-Bell, 2002, Pages 90-93.

[37] R. E. Fischer, B. Tadic-Galeb, P. R. Yoder. *Optical system design,* McGraw-Hill Education, 2008, Pages 49-54.

[38] J. E. Greivenkamp. *Field guide to geometrical optics,* SPIE, FG01, 2004, Page 79.

[39] Ibid. Pages 80-81.

[40] J. Sasián. *Introduction to aberrations in optical imaging systems,* Cambridge University Press, 2013, Page 70.

[41] J. E. Greivenkamp. *Field guide to geometrical optics,* SPIE, FG01, 2004, Page 89.

[42] Ibid. Page 75.

[43] R. E. Fischer, B. Tadic-Galeb, P. R. Yoder. *Optical system design,* McGraw-Hill Education, 2008, Pages 89-90.

[44] Ibid. Pages 191-198.

[45] Ibid. Pages 144-145.

[46] Ibid. Pages 189-191.

[47] K. Schwertz, J. Burge, *Field Guide to Optomechanical Design and Analysis*, SPIE, FG26, 2012, Page 115.